Draft version January 23, 2022
Typeset using LaTeX **twocolumn** style in AASTeX62

arXiv:1905.11685v3 [astro-ph.SR] 19 Jul 2019

Three-dimensional simulation of the fast solar wind driven by compressible magnetohydrodynamic turbulence

Munehito Shoda,[1,2] Takeru Ken Suzuki,[3] Mahboubeh Asgari-Targhi,[4] and Takaaki Yokoyama[2]

[1] *National Astronomical Observatory of Japan, National Institute of Natural Sciences, 2-21-1 Osawa, Mitaka, Tokyo, 181-8588, Japan*
[2] *Department of Earth and Planetary Science, The University of Tokyo, 7-3-1 Hongo, Bunkyo, Tokyo, 113-0033, Japan*
[3] *School of Arts & Science, The University of Tokyo, 3-8-1 Komaba, Meguro, Tokyo, 153-8902, Japan*
[4] *Harvard–Smithsonian Center for Astrophysics, 60 Garden Street MS-15, Cambridge, MA 02138, USA*

ABSTRACT

Using a three-dimensional compressible magnetohydrodynamic (MHD) simulation, we have reproduced the fast solar wind in a direct and self-consistent manner, based on the wave/turbulence driven scenario. As a natural consequence of Alfvénic perturbations at the coronal base, highly compressional and turbulent fluctuations are generated, leading to heating and acceleration of the solar wind. The analysis of power spectra and structure functions reveals that the turbulence is characterized by its imbalanced (in the sense of outward Alfvénic fluctuations) and anisotropic nature. The density fluctuation originates from the parametric decay instability of outwardly propagating Alfvén waves and plays a significant role in the Alfvén wave reflection that triggers turbulence. Our conclusion is that the fast solar wind is heated and accelerated by compressible MHD turbulence driven by parametric decay instability and resultant Alfvén wave reflection.

Keywords: magnetohydrodynamics (MHD) – methods: numerical – Sun: solar wind – turbulence

1. INTRODUCTION

One of the most important unsolved problems in astrophysics is the driving mechanism of the solar wind. In addition to the close relation to the coronal heating problem (Parker 1958), understanding solar wind acceleration is required for stellar rotational evolution (e.g. Brun & Browning 2017) and for space weather forecasting at Earth and at exoplanets (e.g. Garraffo et al. 2016). It is now widely accepted that the ultimate energy source of the solar wind comes from the surface convection. Only $0.1-1\%$ of the photospheric energy flux is sufficient to drive the solar wind (Withbroe & Noyes 1977). Indeed, some observations confirm the sufficient upward energy transport (De Pontieu et al. 2007; McIntosh et al. 2011), whereas we should note that these observations are still controversial (see e.g. Thurgood et al. 2014). An unsolved issue regarding solar wind acceleration is the thermalization process, specifically the nature of solar wind turbulence where the solar wind is accelerated. In-situ observations near 1 au indicate that the turbulent dissipation (cascading) accounts for ongoing heating of the solar wind plasma against adiabatic expansion (Carbone et al. 2009). However, since the plasma condition is very different between the Earth's orbit ($r/R_\odot \approx 200$ where $R_\odot$ denotes the solar radius) and the wind acceleration region ($r/R_\odot \approx 10$), it is risky to simply assume the same situation. In fact, several observations show that the density fluctuation is large near the Sun ($r/R_\odot \approx 1-10$, see Miyamoto et al. 2014; Hahn et al. 2018).

In this study, based on the wave/turbulence-driven (WTD) scenario (Hollweg 1986; Ofman & Davila 1998; Ofman 2004; Suzuki & Inutsuka 2005; Cranmer et al. 2007; Verdini et al. 2010; Chandran et al. 2011; Cranmer 2012), we perform three-dimensional, compressible MHD simulation of the fast solar wind. The simulation is conducted in a self-consistent manner; direct calculation of MHD equations enables us to consider the evolutions of the mean field and fluctuation simultaneously. The compressibility is critical for two reasons. First, due to the compression of plasma, formation of shock waves is allowed, which can contribute to the heating of the solar wind (Hollweg 1982; Suzuki & Inutsuka 2005; Matsumoto & Suzuki 2014; Shoda et al. 2018a). Second, the parametric decay instability (PDI) is incorporated. PDI is an instability of Alfvén wave (Galeev &

Corresponding author: Munehito Shoda
shoda@eps.s.u-tokyo.ac.jp

Oraevskii 1963; Sagdeev & Galeev 1969; Goldstein 1978; Derby 1978) and can grow in the wind acceleration region (Suzuki & Inutsuka 2006; Tenerani & Velli 2013; Shoda et al. 2018b; Réville et al. 2018; Chandran 2018) and activate the turbulence by introducing various energy cascading channels (e.g. Shoda & Yokoyama 2018). In fact, some have found that reduced MHD model cannot account for the solar wind heating without density fluctuation (Perez & Chandran 2013; van Ballegooijen & Asgari-Targhi 2016; Verdini et al. 2019) that is likely to be generated by PDI. In addition to the compressibility, three-dimensionality is crucial for solving turbulence. In general, lower-dimensional (1D or 2D) simulations show different behavior compared with 3D ones (e.g. Shoda & Yokoyama 2018). Therefore, both compressibility and three-dimensionality appear to be crucial for the study of solar wind turbulence.

2. METHOD

We simulate the fast solar wind from the polar region in the solar minimum. The basic equations are ideal MHD equations with gravity and thermal conduction in the spherical coordinates:

$$\frac{\partial}{\partial t}\rho + \nabla\cdot(\rho\boldsymbol{v}) = 0, \tag{1}$$

$$\frac{\partial}{\partial t}(\rho\boldsymbol{v}) + \nabla\cdot\left(\rho\boldsymbol{v}\boldsymbol{v} + p_T\hat{\boldsymbol{I}} - \frac{\boldsymbol{B}\boldsymbol{B}}{4\pi}\right) = \rho\boldsymbol{g}, \tag{2}$$

$$\frac{\partial}{\partial t}\boldsymbol{B} + \nabla\cdot(\boldsymbol{v}\boldsymbol{B} - \boldsymbol{B}\boldsymbol{v}) = 0, \tag{3}$$

$$\frac{\partial}{\partial t}e + \nabla\cdot\left[(e+p_T)\,\boldsymbol{v} - \frac{\boldsymbol{B}}{4\pi}(\boldsymbol{v}\cdot\boldsymbol{B}) + \boldsymbol{q}_{\rm cnd}\right] = \rho\boldsymbol{g}\cdot\boldsymbol{v}, \tag{4}$$

where

$$e = \frac{p}{\gamma-1} + \frac{1}{2}\rho\boldsymbol{v}^2 + \frac{\boldsymbol{B}^2}{8\pi}, \quad p_T = p + \frac{\boldsymbol{B}^2}{8\pi}. \tag{5}$$

See, for example, Matsumoto et al. (2016) for the notations of variables. $\hat{\boldsymbol{I}}$ stands for the unit tensor, $\boldsymbol{g}$ and $\boldsymbol{q}_{\rm cnd}$ are the gravitational acceleration and thermal conductive flux, respectively. We employ the adiabatic specific heat ratio of monatomic gas $\gamma = 5/3$. In solving these equations, the spherical coordinate system is used on the $\theta = \pi/2$ plane that symmetrizes θ and ϕ with respect to ∇ operator as

$$\nabla \approx \boldsymbol{e}_r\frac{\partial}{\partial r} + \boldsymbol{e}_\theta\frac{1}{r}\frac{\partial}{\partial\theta} + \boldsymbol{e}_\phi\frac{1}{r}\frac{\partial}{\partial\phi}, \tag{6}$$

where $\boldsymbol{e}_{r,\theta,\phi}$ denotes the unit vector in each direction. Due to the small horizontal (θ and ϕ) extension of our numerical domain, this approximation yields at most 0.1% error compared with the usual spherical coordinate. Note that we replace $r\sin\theta$ with r in Eq. (6) and the deviation between the two is in the order of $(\theta-\pi/2)^2$ near $\theta = \pi/2$, which yields 10^{-3} in our setting. Since we are simulating polar wind, $\boldsymbol{g}$ is given as

$$\boldsymbol{g} = -\frac{GM_\odot}{r^2}\boldsymbol{e}_r. \tag{7}$$

The radiative cooling is not considered because we do not solve the atmosphere below the transition region where radiation plays a role. The thermal conduction instead dominates the energy balance in the corona and solar wind. We employ a conductive flux that mimics the Spitzer-Härm type one (Spitzer & Härm 1953) as

$$\boldsymbol{q}_{\rm cnd}\cdot\boldsymbol{e}_r = -\kappa_0\xi(r)T^{5/2}\hat{b}_r^2\frac{\partial T}{\partial r}, \tag{8}$$

$$\boldsymbol{q}_{\rm cnd}\cdot\boldsymbol{e}_\theta = -\kappa_0\xi(r)T^{5/2}f_q\hat{b}_\theta^2\frac{1}{r}\frac{\partial T}{\partial\theta}, \tag{9}$$

where $\kappa_0 = 10^{-6}$ in cgs unit, $\xi(r)$ is a quenching due to the large mean free path of electron (Hollweg 1974) and $\hat{b}_{r,\theta,\phi} = B_{r,\theta,\phi}/|\boldsymbol{B}|$. ϕ component of $\boldsymbol{q}_{\rm cnd}$ is given in a similar way as θ component. The quenching term $\xi(r)$ is given as a function of r:

$$\xi(r) = \min\left(1, \frac{r_{\rm sw}^2}{r^2}\right), \tag{10}$$

where $r_{\rm sw} = 5R_\odot$ in this study. Note that Eq. (10) yields much stronger conduction quenching compared with observation. Only a few reduction from Spitzer-Härm value is observed in the solar wind (Bale et al. 2013; Verscharen et al. 2019). The $1/r^2$ dependence of $\xi(r)$ is for numerical reason; such $\xi(r)$ makes the thermal diffusivity $\left(\propto \xi(r)T^{5/2}/\rho\right)$ almost constant in r. In the future, we will compute additional models with full Spitzer-Harm conduction and compare the results with the approximate version used here. An additional quenching $f_q = 0.1$ is used to avoid the severe restriction of time step. Numerical results do not depend on the value of f_q because the conductions in θ and ϕ directions are sufficiently fast to homogenize the temperature on the horizontal plane. Although the conductive flux in our model is not the same as Spitzer-Härm type one, the most important effect of thermal conduction, that is cooling by the radial heat transport, is appropriately solved. Thus, our simplified conductive flux is appropriate for the solar wind simulation.

The numerical domain extends from the coronal base ($r = 1.02R_\odot$) to $r = 20R_\odot$ with horizontal size 20 Mm at the bottom, which yields the range of θ and ϕ as

$$-1.44\times10^{-2}\ \text{rad} \le \theta,\ \phi \le 1.44\times10^{-2}\ \text{rad}. \tag{11}$$

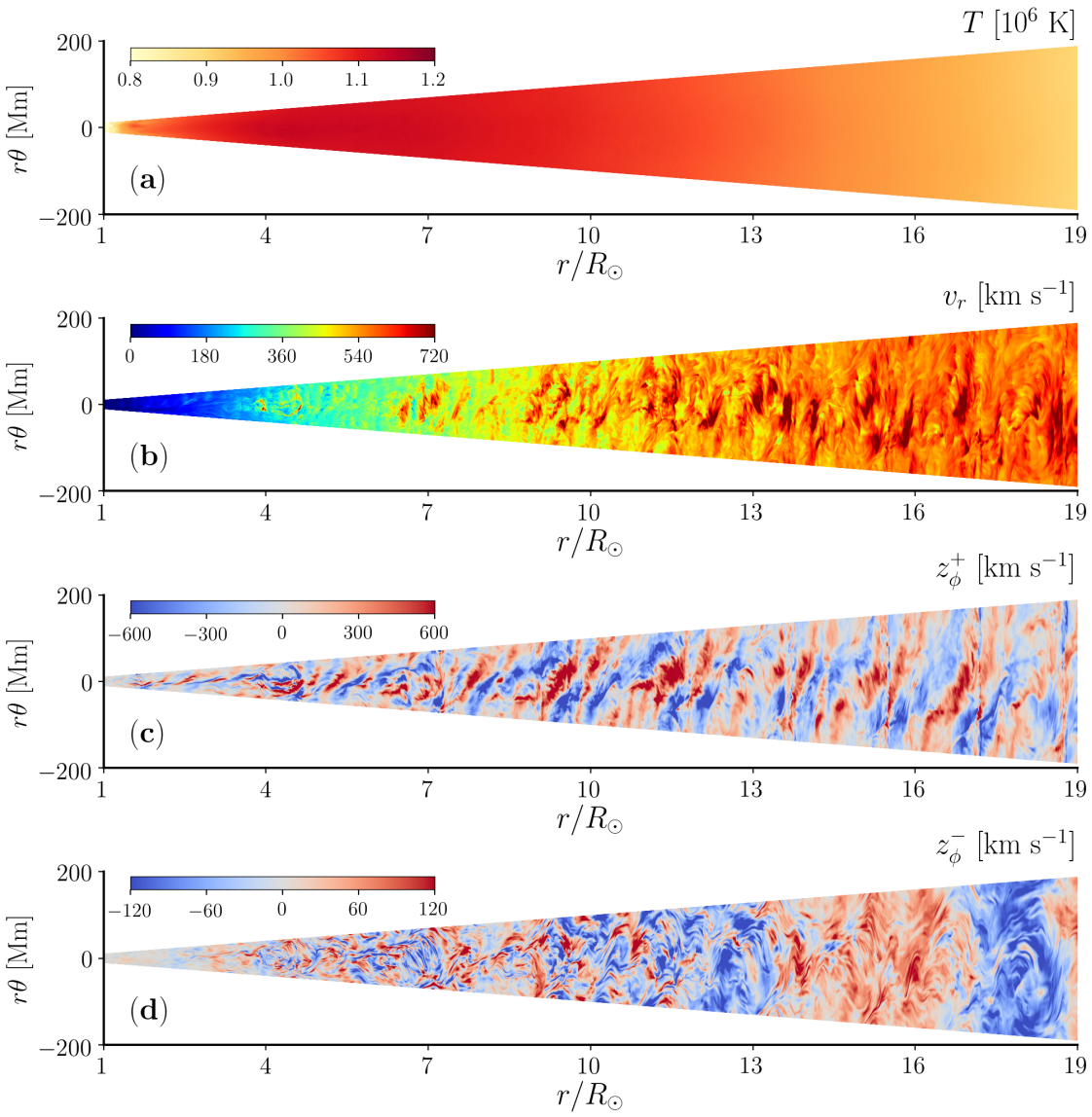


Figure 1. Snapshots on the meridional ($\phi = 0$) plane in the quasi-steady state. Each panel corresponds to (a): temperature, (b): radial velocity, (c): anti-Sunward Elsässer variable and (d): Sunward Elsässer variable, respectively. An animation of this figure is available in the online journal.

An additional numerical domain with coarser grids is prepared beyond the top boundary up to $r \approx 10^3 R_\odot$, far enough to ensure that no fluctuations reach within the time of simulation. This method is validated because no physical quantities can propagate back, against the super-Alfvénic solar wind, to the numerical domain in the quasi-steady state. As an initial condition, we impose the isothermal Parker wind with temperature $T = 1.1 \times 10^6$ K with radially extending magnetic field embedded. The bottom boundary is as follows. The density, temperature and radial magnetic field are fixed to $\rho = 8.5 \times 10^{-16}$ g cm^{-3}, $T = 6 \times 10^5$ K and $B_r = 2$ G, respectively, without any variation in θ and ϕ directions. We note that the mass-loss rate of the solar wind is basically controlled by the physical condition at the inner boundary. In our future study, we take into account the energy transfer from the chromosphere through the transition region, which can determine the mass loss rate in a more self-consistent manner. (Cranmer & Saar 2011; Suzuki et al. 2013). If we consider the expansion factor of magnetic field, $B_r = 2$ G is consistent with the source of the fast solar wind (Fujiki et al. 2015), since in the quasi-steady state of our simulation, the global magnetic field configuration is radial at any given time.

The radial derivative of v_r is fixed to zero, which allows the supply of mass into the numerical domain. The inward Elsässer variables $z^-_{\theta,\phi}$ are set to be transmissive at the bottom. Here the upward ($z^+_\perp$) and downward ($z^-_\perp$) Elsässer variables are defined as

$$\boldsymbol{z}^\pm_\perp = z^\pm_\theta \boldsymbol{e}_\theta + z^\pm_\phi \boldsymbol{e}_\phi, \quad z^\pm_{\theta,\phi} = v_{\theta,\phi} \mp \frac{B_{\theta,\phi}}{\sqrt{4\pi\rho}}. \tag{12}$$

The amplitude of the upward Elsässer variable at the bottom boundary is 64 km s^{-1} corresponding to the observed non-thermal velocity of 32 km s^{-1} (e.g. Banerjee et al. 2009; Landi & Cranmer 2009). For spatial and temporal profiles of the injected Elsässer variables, we impose f^{-1} spectrum in the range of 10^{-3} Hz $\leq f \leq 10^{-2}$ Hz for time variation and $k_\perp^{-2}$ spectrum in the range of $2\pi/(20\ \mathrm{Mm}) \leq k_\perp \leq 6\pi/(20\ \mathrm{Mm})$ for spatial variation. Note that 20 Mm is the horizontal scale of the simulation domain at the bottom. The typical horizontal length scale of the upward Elsässer variable is fixed to the horizontal size of the simulation domain. The basic equations are numerically integrated by the combination of 3rd-order SSP Runge–Kutta method (Shu & Osher 1988) and HLLD Riemann solver (Miyoshi & Kusano 2005) with spatial reconstruction a combination of 2nd-order MUSCL (van Leer 1979) and 5th-order MP5 (Suresh & Huynh 1997) methods. The number of grid points is $(6600, 192, 192)$ in (r, θ, ϕ) directions, respectively. The super-time-stepping method is used to solve the thermal conduction (Meyer et al. 2014). To remove the numerically generated finite $\nabla \cdot \boldsymbol{B}$, we employ the hyperbolic cleaning method (Dedner et al. 2002).

3. RESULTS & DISCUSSION

Figure 1 shows the snapshots of temperature (Panel **a**), radial velocity (Panel **b**), anti-Sunward Elsässer variable (Panel **c**) and Sunward Elsässer variable (Panel **d**), respectively, on the meridional plane after the quasi-steady state is achieved. The maximum temperature exceeds 10^6 K and the termination radial velocity approximates 600 km s^{-1}, ensuring the successful reproduction of the fast solar wind. As a natural consequence of fast thermal conduction, no fine structuring is observed in the temperature map. The panel of v_r shows that, in addition to the gradual acceleration of the solar wind, ubiquitous local (or discontinuous) enhancements are observed. According to the previous 1D simulations (Suzuki & Inutsuka 2005; Shoda et al. 2018a), these fluctuations are large-amplitude slow mode waves that can at least partially contribute to the heating of the solar wind.

Panels **c** and **d** in Figure 1 show the evolution of waves and turbulence. Note that z^+_ϕ and z^-_ϕ correspond to anti-Sunward and Sunward Alfvén wave characteristics in the linear regime. z^+_ϕ maintains the coherent structure in the entire simulation domain while z^-_ϕ shows an evidence of strong turbulent distortion. It is evident, especially in $4 \lesssim r/R_\odot \lesssim 10$, that z^-_ϕ has much finer transverse structure than z^+_ϕ. This feature is more quantitatively observed in the Elsässer power spectra with respect to perpendicular wave number defined as

$$\int E^\pm(k_\perp)\, dk_\perp = \frac{1}{L_\perp^2} \int r^2 d\theta d\phi\ \boldsymbol{z}^2_\perp(\theta, \phi), \tag{13}$$

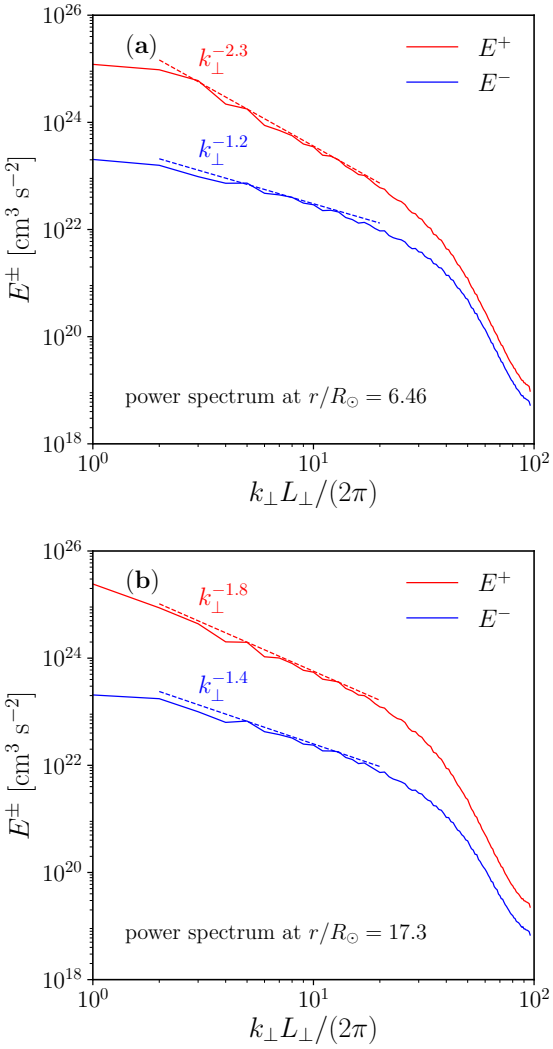


Figure 2. Omnidirectional Elsässer power spectra with respect to perpendicular wave number. The top and bottom panels correspond to the radial distances of $r/R_\odot = 6.46$ and $r/R_\odot = 17.3$, respectively. Solid lines indicate the spectra of anti-Sunward (E^+, red) and Sunward (E^-, blue) Elsässer variables, respectively. Power-law-fitted lines in the inertial range are shown by the dashed lines.

where $k_\perp$ is the wave number perpendicular to the mean field direction (r axis) and $L_\perp$ denotes the horizontal extension of the simulation domain at r. Note that $E^\pm(k_\perp)$ reflects the spatial structures of anti-Sunward and Sunward Elsässer variables perpendicular to the mean field. Solid lines in Figure 2 show $E^\pm(k_\perp)$ calculated at $r/R_\odot = 6.46$ (Panel **a**) and $r/R_\odot = 17.3$ (Panel **b**). Also shown by dashed lines correspond to the power-law fitting in the inertial range ($2 \le k_\perp L_\perp/(2\pi) \le 20$). We observe different inertial-range power indices between E^+ and E^- for both locations. Specifically, the anti-Sunward component has flatter (harder) power spectrum than that of Sunward one. This spectral behavior is consistent with structure difference between z^+_ϕ and z^-_ϕ observed in Figure 1, because the flatter power spectrum is associated with finer structures. Note that similar power spectra of $E^\pm$ are found in imbalanced incompressible MHD turbulence (Chandran 2008). Another interesting feature is that, as r gets larger, the power indices of both E^+ and E^- approach the Kolmogorov's index $-5/3$, which is observed in the magnetic power spectrum in the solar wind (e.g. Bruno & Carbone 2013). See below for additional discussion of the turbulence physics.

A brief description of the spectral difference is given as follows. In the regime of reduced MHD, neglecting the inhomogeneity of the background, the evolution of Alfvén waves is described as follows (e.g. Priest 2014):

$$\frac{\partial}{\partial t}\boldsymbol{z}^\pm + \left(\boldsymbol{z}^\mp \cdot \nabla\right)\boldsymbol{z}^\pm = 0, \quad \boldsymbol{z}^\pm = \boldsymbol{v} \mp \boldsymbol{B}/\sqrt{4\pi\rho}. \quad (14)$$

Thus, the nonlinear wave-wave interaction is invoked by the collision of counter-propagating waves. Note, however, that, in the presence of background inhomogeneity, this is not the case because Elsässer variables are no longer pure characteristics of Alfvén waves (anomalous components, see Velli et al. 1989; Velli 1993; Perez & Chandran 2013). Eq. (14) shows that the energy cascading timescale of $z^\pm$ is determined by $z^\mp$. Specifically when $z^+ > z^-$, the cascading of z^- proceeds faster than z^+, leading to structure difference (see e.g. Chandran et al. 2015). In terms of relaxation process, this process is called dynamical alignment (e.g. Biskamp 2003), in which the minor component of $z^\pm$ decays faster than the major one.

More quantitative explanation of the spectral imbalance is also given both numerically and analytically. The theory and simulation of the incompressible MHD turbulence show (Boldyrev & Perez 2009)

$$E^\pm \propto k_\perp^{-2\pm\alpha}, \quad (15)$$

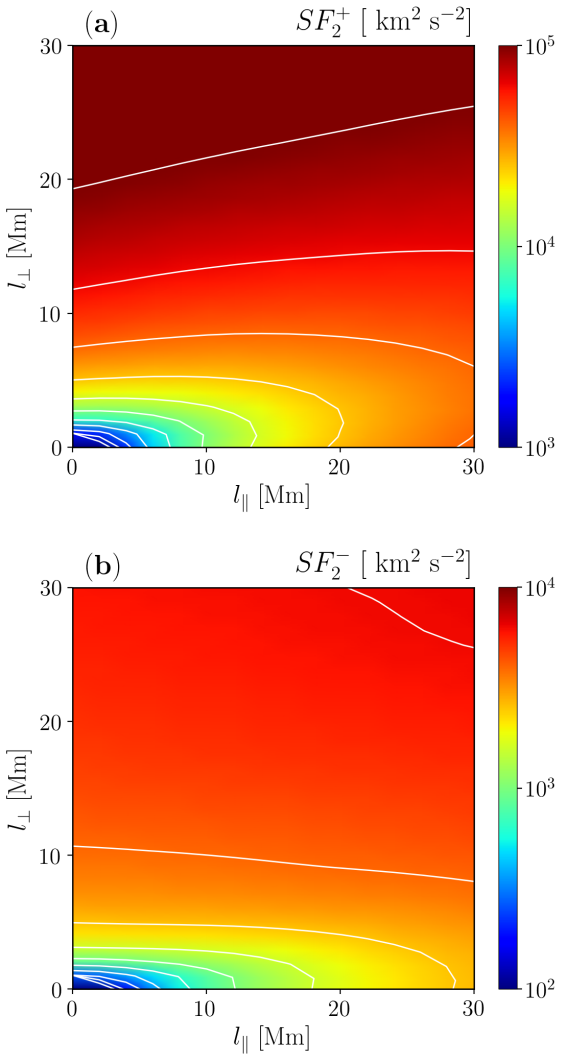


Figure 3. 2nd-order structure function of anti-Sunward (SF_2^+, top) and Sunward (SF_2^-, bottom) Elsässer variables measured in the vicinity of $r/R_\odot = 10$. Embedded white lines represent the contour lines.

while the strong turbulence (EDQNM) theory predicts (Grappin et al. 1983)

$$E^\pm \propto k_\perp^{-3/2\pm\tilde{\alpha}}, \quad (16)$$

where α and $\tilde{\alpha}$ depend on the degree of imbalance E^+/E^-. Compressible MHD turbulence also possibly exhibits the similar spectral difference (Perez et al. 2012). Though not perfectly, our results are at least qualitatively consistent with these predictions. The summation of power indices shifts from -3.5 ($r/R_\odot = 6.46$) to -3.2 ($r/R_\odot = 17.3$), suggesting the weak-to-strong transition of turbulence.

The anisotropy is another factor that characterizes the structure of turbulence. In the presence of mean magnetic field, the structure of turbulence is expected to be

anisotropic (e.g. Goldreich & Sridhar 1995). To see the degree of anisotropy, we often use the 2nd-order structure function (Cho & Lazarian 2003; Verdini et al. 2015) defined as

$$SF_2^{\pm}\left(l_{\parallel}, l_{\perp}\right) = \left\langle \left| \boldsymbol{z}_{\perp}^{\pm}\left(\boldsymbol{x} + l_{\parallel}\boldsymbol{e}_r + l_{\perp}\boldsymbol{e}_{\theta}\right) - \boldsymbol{z}_{\perp}^{\pm}\left(\boldsymbol{x}\right)\right|^2 \right\rangle \tag{17}$$

where the bracket denotes the averaging operator over θ, ϕ and t. Here the structure function is defined based on two assumptions; the turbulence is anisotropic with respect to r axis and isotropic in the $\theta\phi$ plane. The first assumption is justified since the mean magnetic field is perfectly aligned with r axis. In some simulations of the solar wind, the second assumption is violated because the wind expansion introduces another form of anisotropy (Dong et al. 2014). The flow direction of the solar wind is therefore an additional anisotropy axis that forms 3D anisotropy of the wind turbulence (Verdini et al. 2018). In our calculation, because we simulate the wind from the polar region, the flow direction is aligned with the mean field. The definition of the structure function is justified.

Figure 3 shows $SF_2^{\pm}$ measured at $r/R_{\odot} = 10$. Both SF_2^{+} and SF_2^{-} rapidly increase in $l_{\perp}$ direction, showing that field-aligned structures are generated preferentially in the solar wind. This is consistent with previous works (e.g. Cho & Lazarian 2003; Shoda & Yokoyama 2018). A difference of anisotropy is also observed; the minor component (SF_2^{-}) shows larger degree of anisotropy than the major component (SF_2^{+}). This is consistent with the result of phenomenological study of Alfvén wave turbulence (Beresnyak & Lazarian 2008). We also note that the fluctuations in the solar wind show a similar behavior (Wicks et al. 2011).

The results and discussion above show that the structure of solar wind turbulence is consistent with that of incompressible MHD (Alfvén-wave) turbulence. This does not mean that the compressibility is ignorable in the solar wind. In fact, the density fluctuation appears to be required to account for the heating rate in the solar wind (van Ballegooijen & Asgari-Targhi 2016). Specifically, the density fluctuations act as reflectors of anti-Sunward Alfvén waves, playing an indirect but critical role in the onset of turbulence. Figure 4 shows the distribution, origin and role of density fluctuation. Panel (a) shows the turbulent and discontinuous structure of fractional density fluctuation $\delta\rho/\rho$ on the meridional plane. Note that the magnitude of density fluctuation is, at least locally, as large as the mean density. Panel (b) displays the magnitude of root-mean-squared fractional density fluctuation, $\delta\rho_{\rm rms}/\rho$, where

$$\delta\rho_{\rm rms} = \sqrt{\langle\rho^2\rangle - \langle\rho\rangle^2}, \tag{18}$$

and the growth rate of parametric decay instability (PDI) of Alfvén waves, $\gamma_{\rm PDI}$, in unit of mHz. In the accelerating, expanding solar wind, $\gamma_{\rm PDI}$ is given as (Tenerani & Velli 2013; Shoda et al. 2018b)

$$\gamma_{\rm PDI} = \tilde{\gamma}_{\rm GD} 2\pi f_0 - \gamma_{\rm acc} - \gamma_{\rm exp}, \tag{19}$$

where $\tilde{\gamma}_{\rm GD}$ is the normalized growth rate (Goldstein 1978; Derby 1978) in the homogeneous system, $f_0 = 10^{-3}$ Hz is the lowest frequency of the injected Alfvén waves, and $\gamma_{\rm acc}$ and $\gamma_{\rm exp}$ are the suppression of density fluctuation by the wind acceleration and expansion (see Shoda et al. 2018b). Note that we show $\gamma_{\rm PDI}/2$ rather than $\gamma_{\rm PDI}$ for better visualization. A clear spatial correlation between $\gamma_{\rm PDI}$ and $\delta\rho/\rho$ shows that the density fluctuation originates in PDI. Thus the density fluctuation comes from the PDI. Panel (c) shows how the density fluctuation affects the Alfvén wave propagation by displaying the reflection rate of anti-Sunward Alfvén waves given as (Heinemann & Olbert 1980)

$$\omega_{\rm ref} = \left(v_r + v_{A,r}\right)\frac{\partial}{\partial r}\ln\left(r\rho^{1/4}\right), \tag{20}$$

where $v_{A,r} = B_r/\sqrt{4\pi\rho}$. To see the role of density fluctuation, we compare $\omega_{\rm ref}$ calculated in two ways. First, we calculate $\omega_{\rm ref}$ at each given time and space and average it over time and $\theta\phi$ plane. Second, we first average v_r, $v_{A,r}$ and ρ in time and horizontal space, and calculate $\omega_{\rm ref}$ using Eq. (20). The former and latter correspond to the reflection rates with and without density fluctuations, because any fluctuations are smoothed out by averaging the background values (v_r, $v_{A,r}$, ρ). The comparison of these two values are shown in Panel (c). The density fluctuation enhances the reflection rate by a factor of 10 or larger, and therefore the density fluctuation plays a dominant role in the Alfvén wave reflection that triggers turbulence. To summarize, we have shown that the density fluctuation, excited by the PDI, plays a crucial role in the turbulence trigger, and therefore, the compressibility is far from negligible in the solar wind acceleration.

4. CONCLUSION

Our three-dimensional MHD simulation reproduces the fast solar wind as a natural consequence of Alfvén-wave injection from the coronal base, thus supporting the wave/turbulence-driven model of the fast solar wind. The turbulence is characterized by imbalance (Figure 2), anisotropy (Figure 3), and compressibility (Figure 4). The structure of turbulence is well described by the incompressible or reduced MHD turbulence in which the compressibility is ignored. To discuss the turbulent dissipation and heating, however, compressibility plays a

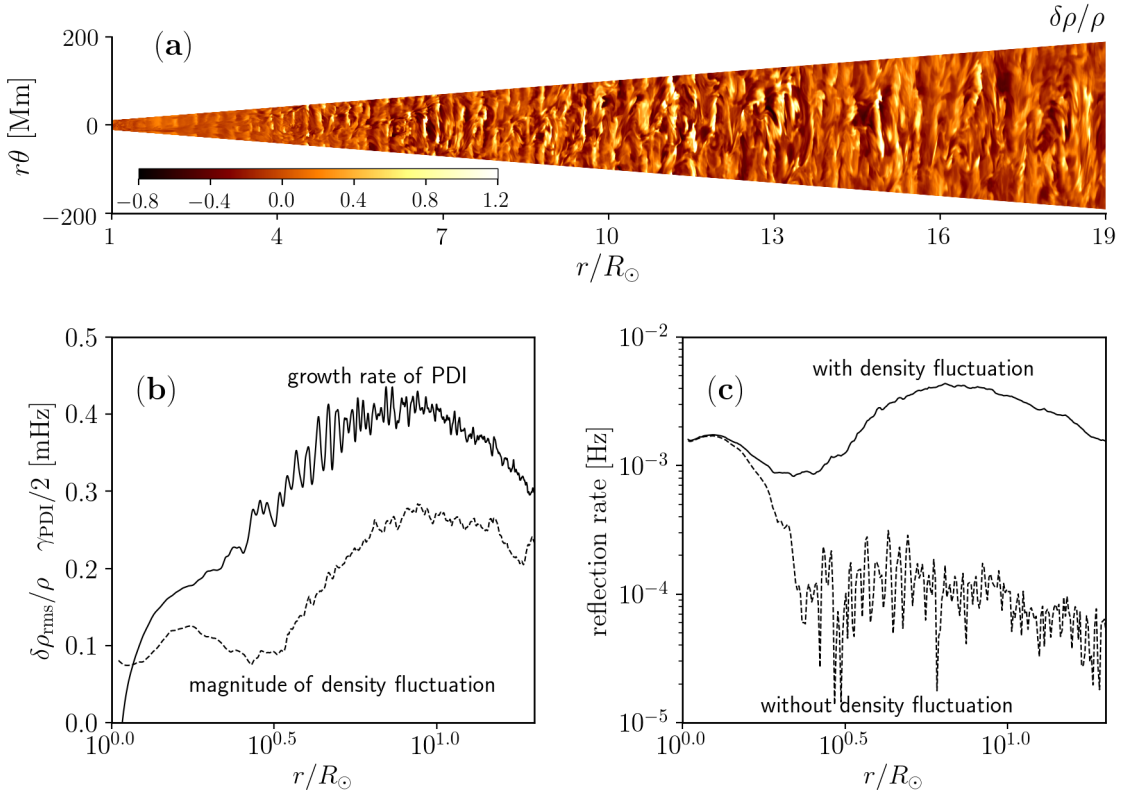


Figure 4. Panel **a**: a snapshot of fractional density fluctuation $\delta\rho/\rho$ in the meridional plane. Panel **b**: growth rate of parametric decay instability ($\gamma_{\rm PDI}/2$, solid line) in unit of mHz and the magnitude of density fluctuation ($\delta\rho/\rho$, dashed line) versus radial distance. Panel **c**: reflection rates of anti-Sunward Alfvén waves $\omega_{\rm ref}$ with and without density fluctuations. An animation of Panel **a** is available in the online journal.

crucial role because the wave reflection, the source of Alfvén wave turbulence, is driven dominantly by density fluctuations excited by the parametric decay instability of Alfvén waves.

We acknowledge the anonymous referee for a number of helpful and constructive comments. We would also like to thank Marco Velli and Takuma Matsumoto for many useful discussions and comments. Numerical computations were carried out on Cray XC50 at Center for Computational Astrophysics, National Astronomical Observatory of Japan. M. Shoda is supported by Grant-in-Aid for Japan Society for the Promotion of Science (JSPS) Fellows and by the NINS program for cross-disciplinary study (Grant Nos. 01321802 and 01311904) on Turbulence, Transport, and Heating Dynamics in Laboratory and Solar/Astrophysical Plasmas: "SoLaBo-X". T.K. Suzuki is supported in part by Grants-in-Aid for Scientific Research from the MEXT of Japan, 17H01105. M. Asgari-Targhi was supported under contract NNM07AB07C from NASA to the Smithsonian Astrophysical Observatory (SAO) and contract SP02H1701R from Lockheed Martin Space and Astrophysics Laboratory (LMSAL) to SAO. T. Yokoyama is supported by JSPS KAKENHI Grant Number 15H03640.

REFERENCES

Bale, S. D., Pulupa, M., Salem, C., Chen, C. H. K., & Quataert, E. 2013, ApJ, 769, L22

Banerjee, D., Pérez-Suárez, D., & Doyle, J. G. 2009, A&A, 501, L15

Beresnyak, A., & Lazarian, A. 2008, ApJ, 682, 1070

Biskamp, D. 2003, Magnetohydrodynamic Turbulence (Cambridge: Cambridge University Press)

Boldyrev, S., & Perez, J. C. 2009, Physical Review Letters, 103, 225001

Brun, A. S., & Browning, M. K. 2017, Living Reviews in Solar Physics, 14, 4

Bruno, R., & Carbone, V. 2013, Living Reviews in Solar Physics, 10, 2
Carbone, V., Marino, R., Sorriso-Valvo, L., Noullez, A., & Bruno, R. 2009, Physical Review Letters, 103, 061102
Chandran, B. D. G. 2008, ApJ, 685, 646
—. 2018, Journal of Plasma Physics, 84, 905840106
Chandran, B. D. G., Dennis, T. J., Quataert, E., & Bale, S. D. 2011, ApJ, 743, 197
Chandran, B. D. G., Schekochihin, A. A., & Mallet, A. 2015, ApJ, 807, 39
Cho, J., & Lazarian, A. 2003, MNRAS, 345, 325
Cranmer, S. R. 2012, SSRv, 172, 145
Cranmer, S. R., & Saar, S. H. 2011, ApJ, 741, 54
Cranmer, S. R., van Ballegooijen, A. A., & Edgar, R. J. 2007, ApJS, 171, 520
De Pontieu, B., et al. 2007, Science, 318, 1574
Dedner, A., Kemm, F., Kröner, D., Munz, C.-D., Schnitzer, T., & Wesenberg, M. 2002, Journal of Computational Physics, 175, 645
Derby, Jr., N. F. 1978, ApJ, 224, 1013
Dong, Y., Verdini, A., & Grappin, R. 2014, ApJ, 793, 118
Fujiki, K., Tokumaru, M., Iju, T., Hakamada, K., & Kojima, M. 2015, SoPh, 290, 2491
Galeev, A. A., & Oraevskii, V. N. 1963, Soviet Physics Doklady, 7, 988
Garraffo, C., Drake, J. J., & Cohen, O. 2016, ApJL, 833, L4
Goldreich, P., & Sridhar, S. 1995, ApJ, 438, 763
Goldstein, M. L. 1978, ApJ, 219, 700
Grappin, R., Leorat, J., & Pouquet, A. 1983, A&A, 126, 51
Hahn, M., D'Huys, E., & Savin, D. W. 2018, ApJ, 860, 34
Heinemann, M., & Olbert, S. 1980, J. Geophys. Res., 85, 1311
Hollweg, J. V. 1974, J. Geophys. Res., 79, 3845
—. 1982, ApJ, 254, 806
—. 1986, J. Geophys. Res., 91, 4111
Landi, E., & Cranmer, S. R. 2009, ApJ, 691, 794
Matsumoto, T., & Suzuki, T. K. 2014, MNRAS, 440, 971
Matsumoto, Y., et al. 2016, arXiv e-prints, arXiv:1611.01775
McIntosh, S. W., de Pontieu, B., Carlsson, M., Hansteen, V., Boerner, P., & Goossens, M. 2011, Nature, 475, 477
Meyer, C. D., Balsara, D. S., & Aslam, T. D. 2014, Journal of Computational Physics, 257, 594
Miyamoto, M., et al. 2014, ApJ, 797, 51
Miyoshi, T., & Kusano, K. 2005, Journal of Computational Physics, 208, 315
Ofman, L. 2004, Journal of Geophysical Research (Space Physics), 109, A07102
Ofman, L., & Davila, J. M. 1998, J. Geophys. Res., 103, 23677
Parker, E. N. 1958, ApJ, 128, 664
Perez, J. C., & Chandran, B. D. G. 2013, ApJ, 776, 124
Perez, J. C., Mason, J., Boldyrev, S., & Cattaneo, F. 2012, Physical Review X, 2, 041005
Priest, E. 2014, Magnetohydrodynamics of the Sun (Cambridge: Cambride University Press)
Réville, V., Tenerani, A., & Velli, M. 2018, ApJ, 866, 38
Sagdeev, R. Z., & Galeev, A. A. 1969, Nonlinear Plasma Theory (New York: Benjamin)
Shoda, M., & Yokoyama, T. 2018, ApJL, 859, L17
Shoda, M., Yokoyama, T., & Suzuki, T. K. 2018a, ApJ, 853, 190
—. 2018b, ApJ, 860, 17
Shu, C.-W., & Osher, S. 1988, Journal of Computational Physics, 77, 439
Spitzer, L., & Härm, R. 1953, Physical Review, 89, 977
Suresh, A., & Huynh, H. T. 1997, Journal of Computational Physics, 136, 83
Suzuki, T. K., Imada, S., Kataoka, R., Kato, Y., Matsumoto, T., Miyahara, H., & Tsuneta, S. 2013, PASJ, 65, 98
Suzuki, T. K., & Inutsuka, S.-i. 2005, ApJL, 632, L49
Suzuki, T. K., & Inutsuka, S.-I. 2006, Journal of Geophysical Research (Space Physics), 111, 6101
Tenerani, A., & Velli, M. 2013, Journal of Geophysical Research (Space Physics), 118, 7507
Thurgood, J. O., Morton, R. J., & McLaughlin, J. A. 2014, ApJL, 790, L2
van Ballegooijen, A. A., & Asgari-Targhi, M. 2016, ApJ, 821, 106
van Leer, B. 1979, Journal of Computational Physics, 32, 101
Velli, M. 1993, A&A, 270, 304
Velli, M., Grappin, R., & Mangeney, A. 1989, Physical Review Letters, 63, 1807
Verdini, A., Grappin, R., Alexandrova, O., & Lion, S. 2018, ApJ, 853, 85
Verdini, A., Grappin, R., Hellinger, P., Landi, S., & Müller, W. C. 2015, ApJ, 804, 119
Verdini, A., Grappin, R., & Montagud-Camps, V. 2019, SoPh, 294, 65
Verdini, A., Velli, M., Matthaeus, W. H., Oughton, S., & Dmitruk, P. 2010, ApJL, 708, L116
Verscharen, D., Klein, K. G., & Maruca, B. A. 2019, arXiv e-prints, arXiv:1902.03448
Wicks, R. T., Horbury, T. S., Chen, C. H. K., & Schekochihin, A. A. 2011, Physical Review Letters, 106, 045001
Withbroe, G. L., & Noyes, R. W. 1977, ARA&A, 15, 363